Visible and ultraviolet upconversion and near infrared downconversion luminescence from lanthanide doped $La_2Zr_2O_7$ nanoparticles

Santosh K. Gupta[a,b], Mitzy A. Penilla Garcia[a], Jose P. Zuniga[a], Maya Abdou[a], Yuanbing Mao[a,c,*]

[a] Department of Chemistry, University of Texas Rio Grande Valley, 1201 West University Drive, Edinburg, TX 78539, USA
[b] Radiochemistry Division, Bhabha Atomic Research Centre, Trombay, Mumbai, 400085, India
[c] School of Earth, Environmental, and Marine Sciences, University of Texas Rio Grande Valley, 1201 West University Drive, Edinburg, TX 78539, USA

ARTICLE INFO

ABSTRACT

Single materials which have a multitude of photophysical processes by selective doping are in high demand in the community of material science due to their multifunctional applications. Upconversion (UC) and down-conversion (DC) luminescence properties of lanthanide doped nanoparticles (NPs) are imperative for their broad application potentials. Here, we describe two series of either doubly or triply doped $La_2Zr_2O_7$ NPs synthesized by a molten salt method. For the former, $La_2Zr_2O_7$:Yb,Er NPs display bright red and moderate green UC (VUC) and NIR-B DC (NDC) at around 1550 nm, which are highly desirable for in-vivo bioimaging applications. For the latter, $La_2Zr_2O_7$:Gd,Yb,Tm NPs demonstrate ultraviolet UC (UVUC) which can be exploited for water purification. In addition, we systematically investigated the effects of sensitizer doping level on the morphology, crystal structure and UC and DC emission intensity of these NPs. The processes involved in the VUC, NDC and UVUC emissions are evaluated in detail by pump power dependence studies which reveal that the VUC emissions are two-photon processes whereas the UVUC emission is a five-photon absorption process. The mechanisms of all these three luminescence processes have been extensively explained based on energy transfer and f-f transition processes. The idea provided in this work extends the knowledge on doping induced UC and DC luminescence in pyrochlore NPs which show multifunctionalities in light emission properties.

1. Introduction

An upconversion (UC) process involves photons emitted with higher frequency than those being used as pumping photons [1,2]. There are several mechanisms which contribute to UC process: ground state absorption followed by excited-state absorption, sequential energy transfer, combination of the former and the latter, photon avalanche, cooperative UC [3–6]. Near infrared (NIR) to visible UC materials have been in great demand in recent years due to their unique anti-Stoke optical features that can be implemented in three-dimensional displays [7], laser and optical amplifiers [8], solar cells [9], optical data storage [10], bio-technologies [11,12], drug-delivery, biosensor, super resolution microscopy, optical temperature sensors [13,14], etc. At the meantime, IR to UVUC materials have also received intensive attention recently due to the applications of UV light in the areas of water disinfection, microbial inactivation, counterfeit detection, lithography, phototherapy, coating technology, forensics, etc. [15,16].

Currently UC materials face the issue of low luminescence efficiency [17,18]. The selective use of sensitizing and activating ions with close

intermediate-excited states is essential to enhance UC efficiency [19,20]. Proper design and optimization of the interaction between sensitizer and activator ions is needed since UC efficiency is highly dependent on the separation distance of dopants.

Trivalent erbium and ytterbium have been widely used for UC materials [13,17,21–23]. The former is one of the most widely explored activators for UC process as it can be efficiently pumped using 980 nm laser to higher energy levels viz. $^2H_{11/2}$, $^4S_{3/2}$ and $^4F_9$ [24]. The latter is used as a sensitizer to improve the efficiencies and absorptions of 980 nm laser because it only possesses one excited f-electron level to allow a strong and broad absorption band at 980 nm [22]. The Er^{3+}-Yb^{3+} combination has been used to improve absorption cross-section of 980 nm photons because Yb^{3+} ions sensitize Er^{3+} ions to upper energy levels through energy transfer.

Moreover, host materials have been triply doped for NIR excitation to UVUC emission, e.g. Yb^{3+}, Gd^{3+} and Tm^{3+} with different concentrations [16,25–27]. These doping ions have been selected due to their exclusive properties. Tm^{3+} has appropriate metastable levels for UVUC emission through the single transition of $^2F_{7/2} \rightarrow {}^2F_{5/2}$. Yb^{3+} is
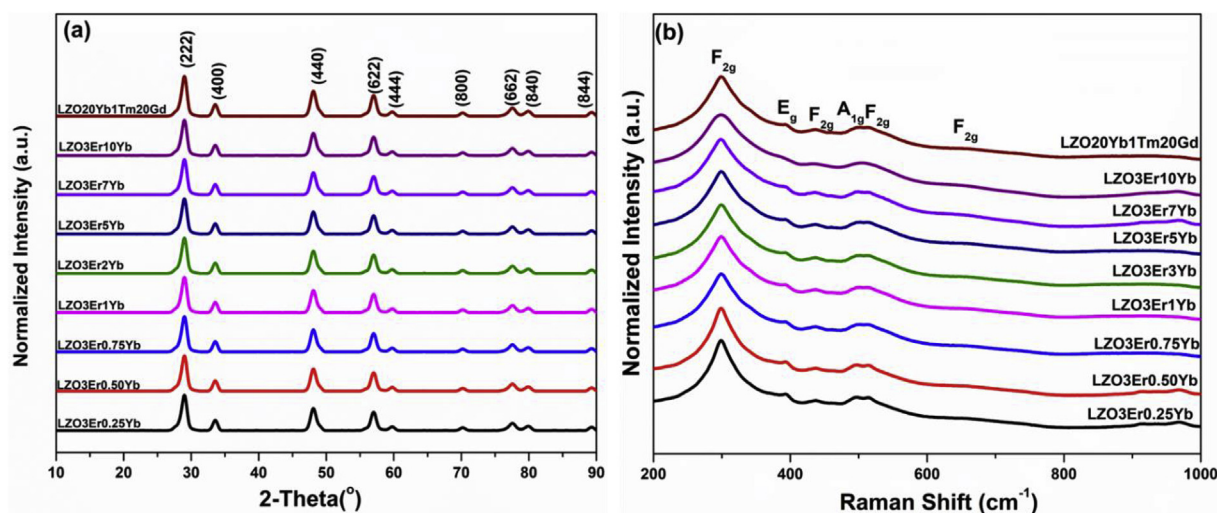
Fig. 1. (a) XRD patterns and (b) Raman spectra of LZO:3%Er,y%Yb NPs at different Yb^{3+} concentrations and LZO:20%Yb,1.0%Tm,20%Gd NPs.

selected as sensitizer for Tm^{3+} activator because of its sole excited energy level to generate large UC improvement and effective UVUC emissions [28–30]. It is difficult to directly populate Gd^{3+} excited energy levels by IR pumping due to the large energy gap between its ground state $^8S_{7/2}$ and the first excited state $^6P_{7/2}$ [16]. To resolve this issue, introduction of Tm^{3+} and Yb^{3+} to Gd^{3+} doped materials offers additional UVUC emissions essential for the development of UV compact devices [31,32].

On the other hand, NIR-A → NIR-B downconversion (DC) luminescent materials absorb the NIR-A light (~700–1000 nm) and emit in the NIR-B region (~1100–1700 nm). This type of materials such as quantum dots (QDs), carbon nanotubes (CNTs) and polymeric nanoparticles (NPs) are potential candidates for deep tissue imaging [33–35]. Such unique characteristics arise from the presence of narrow band gaps of these materials. The reported materials in this class such as CNTs and QDs suffer from the photobleaching problem which is highly undesirable for *in vivo* fluorescence imaging [36]. Another problem with the NIR emitting QDs is that they consist of highly toxic elements such as Pb, As, Hg, etc. [37] CNTs have problems for multi-spectral analysis and disease-specific imaging in the NIR based imaging along with the requirements of high-power pulsed sources (> 2 W) and long camera exposure [38–40]. Moreover, most of the materials in this category emit in the region < 1400 nm (NIR-B1) [34,41]. Materials with emission in the NIR-B2 region (~1500–1600 nm) allow improved *in vivo* bioimaging [34,42]. The NIR-B2 light has deeper penetration and improved resolution because of its optimal balance of photon scattering and H_2O absorption. However, materials emitting in the NIR-B2 region are rarely reported.

$La_2Zr_2O_7$ (LZO) has a pyrochlore structure with wide band gap, high structural stability, high dielectric constant, optimum refractive index, ability of accommodate lanthanide ions easily at both A and B sites, high thermal stability, etc. [43] In addition, it possesses a relatively low phonon energy at ~785 cm^{-1} which minimizes nonradiative relaxation while boosting quantum efficiency [44]. It is reported that $A_2B_2O_7$ type ordered pyrochlores ($Fd\bar{3}m$) undergo phase transition to disordered fluorite phase (Fm-3m) or vice versa by varying temperature, pressure, ionizing radiation, and chemical doping [45–47]. Radius ratio of the A and B cations (r_A/r_B) plays a decisive role between its disordered fluorite (DF) ⇌ ordered pyrochlore (OP) phase transition. The OP phase is stable when the r_A/r_B value is > 1.46 whereas the DF phase is stable when the r_A/r_B value is < 1.46. Both phases have their own advantages: the OP phase is found to be suitable for sensing, scintillator, and thermal barrier coating applications whereas the DF phase is found to be ideal for nuclear waste host and ionic conductor applications [45,46,48,49]. In the literature, aliovalent doping of $A_2B_2O_7$

pyrochlores has induced pyrochlore-to-fluorite/cotunnite structural transition [46,50]. In terms of UC emission, $La_2Zr_2O_7$ has shown red/green UC after replacing Zr by Si [51].

In this work, we report the development of doubly and triply doped LZO nanoparticles (NPs) by a facile molten salt synthesis method [43,46,52,53]. These NPs show efficient VUC and UUC and excellent NIR-B2 emission in the 1475–1600 nm under 980 nm excitation with negligible photobleaching. We have investigated the effects of sensitizer concentration on structure, size and photophysical properties of the doped LZO NPs. Specifically, for the doubly doped $La_2Zr_2O_7$:Yb,Er NPs, we have fixed the Er^{3+} concentration at 3.0% (Figure S1) and varied the Yb^{3+} concentration in the range of 0.25%–10.0%. The reason for this practice stems from the focus for UC relevant studies which have explored the effect of sensitizer ion while keeping the concentration of the main luminophores in the range of 1–3% to avoid concentration quenching [54–57]. For similar reason, for the triply doped $La_2Zr_2O_7$:Gd,Yb,Tm NPs, we have fixed Yb^{3+} concentration at 20%, Tm^{3+} concentration at 1% and Gd^{3+} concentration at 20% [31,32,58]. At the same time, power dependence of UC and DC emission intensity was investigated to give more insight on photon absorption process. The underlying mechanisms of light emission in all three VUC, NDC and UUC processes are explained extensively using energy transfer process and various f-f transitions.

2. Experimental

Synthesis and experimental details are included in the Electronic Supplementary Information.

3. Results and discussion

3.1. X-ray diffraction

XRD patterns of the doubly doped $La_2Zr_2O_7$:Er,Yb NPs with various sensitizer Yb^{3+} concentrations and $La_2Zr_2O_7$:Yb,Tm,Gd NPs (Fig. 1a) showed that no other visible impure phases such as La_2O_3, Yb_2O_3, Er_2O_3, Tm_2O_3, Gd_2O_3 and ZrO_2 were detected. According to the XRD patterns, these samples are assigned to the pure $La_2Zr_2O_7$ phase with ideal pyrochlore structure (JCPDS No. 78–1292) with $Fd\bar{3}m$ space group.

The crystallite size was calculated from the XRD data using the Debye-Scherer formula:

$$d = \frac{k\lambda}{\sqrt{(B_s^2 - B_M^2)}\cos\theta} \tag{1}$$

Table 1
Calculated crystallite size of the LZO:3%Er,y%Yb NPs at different Yb^{3+} concentrations.

Sample	Calculated Crystalline Size (nm)
LZO3Er0.25Yb	22.1 ± 0.9
LZO3Er0.50Yb	20.9 ± 0.9
LZO3Er0.75Yb	19.9 ± 0.9
LZO3Er1Yb	15.0 ± 1.1
LZO3Er2Yb	13.5 ± 1.1
LZO3Er5Yb	12.3 ± 1.2
LZO3Er7Yb	10.9 ± 1.3
LZO3Er10Yb	9.6 ± 1.4
LZO20Yb1Tm20Gd	20.5 ± 0.3

where *d* is the crystallite size, λ is the used X-ray wavelength, θ is the angle of the corresponding Bragg reflection, which is fitted to calculate the full width half maxima (FWHM), *B* is the FWHM in radian, and *K* is the Scherer constant of 0.94 based on cubic crystallites. The FWHM was determined based on the XRD peak (222) with the highest intensity at 28.96° and the fitting was performed using pseudo voigt function. The B_M was calculated using the FWHM value of the highest intensity peak of pure silicon. The calculated crystallite size of the LZO:3%Er,y%Yb NPs (Table 1) decreases with increasing sensitizer concentration. This phenomenon is mainly attributed to the smaller ionic radius of 8-coordinated Yb^{3+} ion (98.6 p.m.) compared to 8-coordinated La^{3+} (116 p.m.).

3.2. Raman spectroscopy

Using common XRD to differentiate structures with similar space group can become difficult. The presence of weak reflections from the ordered pyrochlore phase cannot be ruled out from the XRD patterns of the LZO NPs (Fig. 1a). In this sense, Raman spectroscopy is a more sensitive technique to distinguish the disordered fluoride and ordered pyrochlore structures of LZO by probing metal-oxygen (M − O) vibrational modes [46,52]. A pyrochlore phase has a total of 6 Raman active vibrational modes existing in the wavenumber range of 200–1000 cm^{-1} which are $\Gamma_{OPP} = A_{1g} + E_g + 4F_{2g}$, while the disordered fluorite structure has one active Raman mode that is $\Gamma_{DFP} = F_{2g}$ because all seven O^{2-} ions are randomly oriented over the 8 anionic sites in this particular phase [53,59]. Phase transition from pyrochlore $A_2B_2O_6O'$ P phase ($Fd\bar{3}m$ space group, Z = 8) to fluorite AO_2F structure ($Fm\bar{3}m$, Z = 4) proceeds by the disappearance of A_{1g} and E_g Raman modes and decrease in the number of F_{2g} mode from 4 to 1. The doubly doped LZO:3%Er,y%Yb NPs and the triply doped LZO:20%Yb,1.0%Tm,20%Gd NPs displayed 6 peaks corresponding to ideal pyrochlore structure (Fig. 1b). These peaks are located at 300, 395, 432, 495, 504 and 644 cm^{-1} corresponding to F_{2g}, E_g, F_{2g}, A_{1g}, F_{2g} and F_{2g} modes, respectively [43,60]. The Raman modes at 300, 395 and 432 cm^{-1} arise from the vibrations of the La–O and Zr–O bonds. The bands around 495, 504 and 644 cm^{-1} arise due to the stretching of the Zr–O bonds [45]. The extent of disordering from the LZO:3%Er:y%Yb NPs as a function of Yb^{3+} doping level can be predicted based on the variation of the full width half maxima (FWHM) of the most intense F_{2g} Raman peak
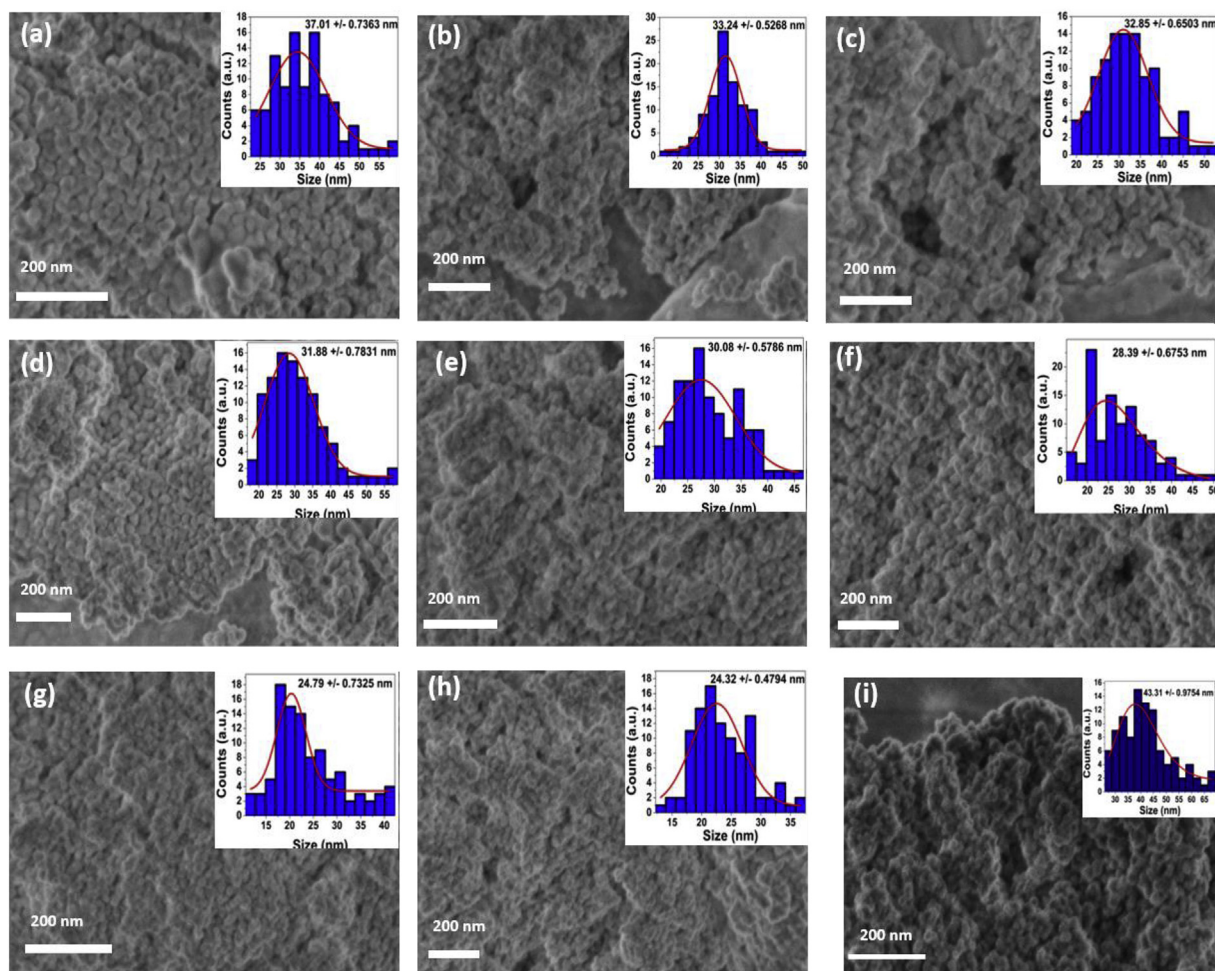

Fig. 2. SEM images of the LZO:3%Er:y%Yb NPs with different Yb^{3+} concentrations of (a) 0.25%, (b) 0.50%, (c) 0.75%, (d) 1.0%, (e) 2.0%, (f) 5.0%, (g) 7.0%, and (h) 10.0%, and (i) the LZO:20%Yb,1.0%Tm,20%Gd NPs.

located around 300 cm^{-1} [45]. The continuous increase of the FWHM value (Fig. 1b) suggests that the ordering extent of our LZO:3%Er:y%Yb NPs with the increasing Yb^{3+} concentration [45]. This phenomenon can be attributed to the tunneling of some Yb^{3+} ion from La^{3+} site to Zr^{4+} site at high Yb^{3+} concentration since the ionic radius of 6-coordinated Zr^{4+} ion is 72 p.m. whereas that of Yb^{3+} ion is 98.6 p.m [52]. Also, the ionic charge of these two ions is different. Such a mismatch of ionic charge and radius creates strain and lattice disordering and hence the broadening of the Raman peak [46,52,53].

3.3. Scanning electron microscopy

SEM was used to monitor the morphological features of the NPs synthesized using the molten-salt method. The doubly doped LZO:3% Er:y%Yb NPs are fine and monodispersed spheres with some extent of agglomeration (Fig. 2a–h). The size is in the range of 10–35 nm, which decreases from 37 nm to 24 nm as the Yb^{3+} concentration increases from 0.25% to 10%. The triply doped LZO:20%Yb,1.0%Tm,20%Gd NPs are spheres with an average size around 43 nm (Fig. 2i).

3.4. PL of the doubly doped LZO: 3%Er:y%Yb NPs

3.4.1. NIR-visible UC

The UC emission spectra of the LZO:Er, Yb NPs were recorded between 500 and 700 nm under 980 nm laser excitation (Fig. 3a). The three prominent peaks around 525, 550 and 660 nm are ascribed to the interconfigurational f–f transitions of Er^{3+}. The dual bands at 525 and 550 nm in the green region are attributed to $^2H_{11/2} \rightarrow {}^4I_{15/2}$ and $^4S_{3/2} \rightarrow {}^4I_{15/2}$ transitions of Er^{3+} ion. The most intense band in the red region around 660 nm is due to $^4F_{9/2} \rightarrow {}^4I_{15/2}$ transition of Er^{3+} ion. No obvious change of the spectral profile was observed as the of Yb^{3+} doping levels increases. This observation suggests that no substantial clustering of Er^{3+} and Yb^{3+} ions happened which could cause deactivation of Er^{3+} excited levels via non-radiative energy transfer [24]. The integral emission intensity ratio of the red and green emission bands varies with Yb^{3+} doping concentration, more specifically, increases initially up to 2.0% and thereafter gradually decreases till 10.0% (inset of Fig. 3a). A comparative UC emission spectrum for LZO:3%Er:y%Yb NPs with different Yb^{3+} concentrations was also performed. In terms of the variation of the red and green emission intensity with Yb^{3+} doping concentration (Fig. 3b), the UC emission intensities increase initially up to 1.0% and thereafter decrease induced by concentration quenching.

When the LZO:3%Er:1%Yb NPs were excited by 980 nm laser with different powers, there is no spectral profile change while the UC emission intensity enhances (Fig. 3c). To predict the number of photons involved for Yb^{3+} to Er^{3+} energy transfer, the UC emission intensity varies with laser power following a relation [61]:

$$I \propto P^n$$

where I is the integral area of a UC emission band, P is the laser power, and n is the number of photons involved in the excitation process and is calculated from the slope of $\log(I)$ vs $\log(P)$ linear plot.

The linear logarithmic plots of the integral area of each UC emission band (525, 550 and 669 nm) and the laser power of the LZO:3%Er:1% Yb NPs (Fig. 3d) show that there are linear relations between the UC intensity as a function of laser power. The slopes of the green emission bands (525 and 550 nm) and red band (660 nm) are approximately 2.0 indicating that two photons are needed to be absorbed by the LZO:3% Er:1%Yb NPs for generating green and red emissions. The correlation coefficient for all the three linear plots was approximately around 0.995 R^2. The CIE color coordinates of the LZO:3%Er:1%Yb NPs at laser power of 2.5 mW (Fig. 3e) with the highest emission output displayed yellowish green emission. There is no much change of either of these two values (Table S1).

The two main UC mechanisms in the excited state populations are energy transfer upconversion (ETU) and excited state absorption (ESA).

Other mechanisms such as an avalanche process or cross-relaxation (CR) between two doped ions may also occur [62]. In general, ESA process is the dominant process for phosphors with low dopant concentrations given that it involves only one ion. On the other hand, ETU is dominant for phosphors with high dopant concentrations because it involves the transfer of energy between two close ions. High doping concentration decreases the average distance between dopant ions which enhances the interionic interaction [55].

The energy levels diagram of Er^{3+} and Yb^{3+} ions with the proposed UC processes of the LZO:Er^{3+},Yb^{3+} NPs is shown in Fig. 3f. Energy transfer from Yb^{3+} to Er^{3+} makes the largest contribution to the emission energy levels because Yb^{3+} has a large absorption cross section at the NIR region and a high doping concentration. Specifically, after absorbing 980 nm photon, Yb^{3+} ions go to excited $^2F_{5/2}$ state and then relax to $^4I_{11/2}$ level of Er^{3+} ions through energy transfer (ETU) due to the close energy between these two states. The absorption of the second photon cause the excitation of electron from $^4I_{11/2}$ level of Er^{3+} to $^4F_{7/2}$ levels. Then the electrons at the high energy $^4F_{7/2}$ state decay nonradiatively to lower levels dissipating 525 and 550 nm green light from $^2H_{11/2}$ and $^4S_{3/2}$ respectively and red emission from states $^4F_{9/2}$.

Moreover, the red emission from the $^4F_{9/2}$ energy level is associated with two different processes. The first process is a nonradiative transition from $^4S_{3/2} \rightarrow {}^4F_{9/2}$ as described above. The second process is the population of $^4I_{13/2}$ level through nonradiative transitions of $^4I_{11/2} \rightarrow {}^4I_{13/2}$, then the latter excited state is further promoted to $^4F_{9/2}$ level either through an ET process as $^2F_{5/2}$ (Yb^{3+}) + $^4I_{13/2}$ (Er^{3+}) $\rightarrow {}^2F_{7/2}$ (Yb^{3+}) + $^4F_{9/2}$ (Er^{3+}) or an ESA process as photon + $^4I_{13/2}$ (Er^{3+}) $\rightarrow {}^4I_{15/2}$(Er^{3+}) + $^4F_{9/2}$(Er^{3+}) [63].

3.4.2. NIR-A to NIR-B DC

The process which involves NIR excitation and NIR fluorescence in the short wave infrared region (SWIR) is an excellent optical probe for fluorescence based in-vivo bioimaging [35,36,38,39,42]. Apart from the UC visible emissions in green and red regions, our LZO:Er, Yb NPs show intense broad spectral band around 1550 nm in NIR-B region under 980 nm excitation. For example, the LZO:3%Er:y%Yb NPs show intense broad NIR-B emission around 1550 nm which is split into several peaks (Fig. 4a). Such NIR-B emission peak is attributed to $^4I_{13/2} \rightarrow {}^4I_{15/2}$ transition of Er^{3+} (Fig. 3f) and the large Stark splitting is cause by crystalline LZO environment [24]. Such DC process involves the excitation of Yb^{3+} by 980 nm photons from its ground $^2F_{7/2}$ level to its single excited $^2F_{5/2}$ level which relaxes to $^4I_{11/2}$ level of Er^{3+} ion through ET. High energy states decay nonradiatively to lower $^4I_{13/2}$ level of Er^{3+} ion followed with emission at 1550 nm due to electronic transition from $^4I_{13/2}$ to $^4I_{15/2}$ [64]. Moreover, the DC emission intensity increases with increasing Yb^{3+} concentration up to 5.0 mol% of Yb^{3+} and then gradually decreases due to concentration quenching (Fig. 4b).

3.5. PL of the triply doped LZO:Yb,Tm,Gd NPs

The LZO:20%Yb,1%Tm,20%Gd NPs displayed UV UC fluorescence under 980 nm excitation (Fig. 5a). The emission peak centered at 289 nm is assigned to the $^3P_0/^1I_6 \rightarrow {}^3H_6$ transition of Tm^{3+}. Emissions peaked at 296, 300, 306 nm are originated from $^6P_{7/2} \rightarrow {}^8S_{7/2}$, $^6P_{5/2} \rightarrow {}^8S_{7/2}$ and $^6P_{3/2} \rightarrow {}^8S_{7/2}$ transitions of Gd^{3+} ion, respectively [32].

Fig. 5b shows the energy levels diagram of the Yb^{3+}, Gd^{3+}, and Tm^{3+} co-doped LZO NPs excited by a 980 nm laser. Here, NIR photons are absorbed by the Yb^{3+} ions, follwed by an ET to populate the $^3H_5$, $^3F_3$ ($^3F_2$) and $^1G_4$ levels of Tm^{3+} [32]. The $^1D_2$ level of Tm^{3+}, however, is populated through cross-relaxation $^3F_3 \rightarrow {}^3H_6 : {}^3F_3 \rightarrow {}^1D_2$ (Tm^{3+}). It can not be directly populated through the ET of $^2F_{5/2} \rightarrow {}^2F_{7/2}$ (Yb^{3+}) : $^1G_4 \rightarrow {}^1D_2$ (Tm^{3+}) because of the large energy mismatch (around 3500 cm^{-1}) [65]. After that, the energy transfer $^2F_{5/2} \rightarrow {}^2F_{7/2}$ (Yb^{3+}) : $^1D_2 \rightarrow {}^3P_{2,1}$ (Tm^{3+}) populates the $^3P_{2,1}$ (Tm^{3+}) levels, which then it decays nonradiatively to $^1I_6$, and $^3P_0$ (Tm^{3+}) levels [66]. This is
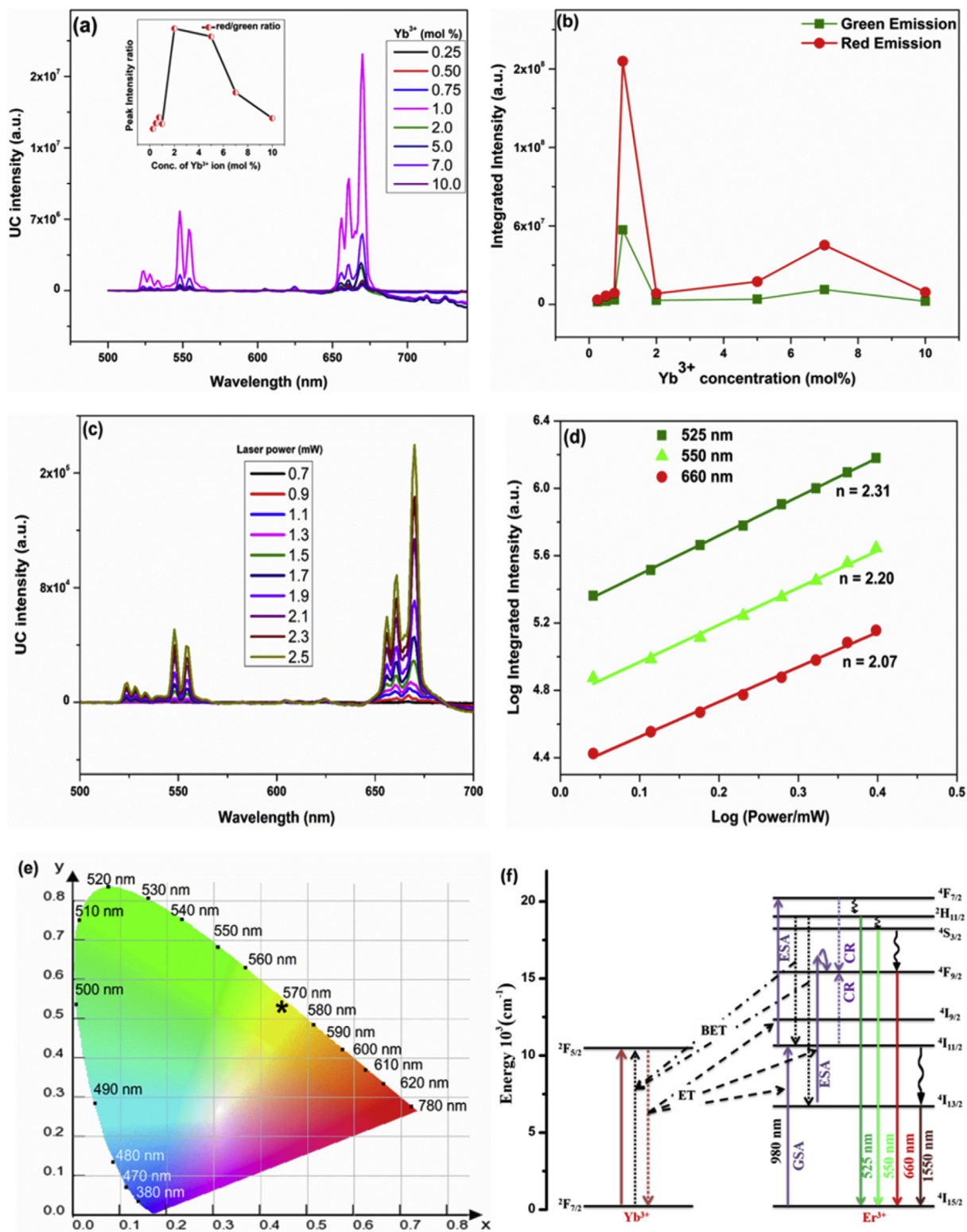
Figure 3. The LZO:Er,Yb NPs: (a) UC emission spectra and (b) variation of UC emission intensity as a function of Yb^{3+} doping concentration. The LZO:3%Er^{3+}:1% Yb^{3+} NPs: (c) UC emission spectra at different laser power, (d) log–log plot of UC emission intensity versus laser power for three emissions bands at 600 nm (square symbol), 550 nm (sphere) and 525 nm (triangle), and (e) CIE chromaticity diagram and (x,y) color coordinates (star mark). (f) Energy level diagram of Er^{3+} and Yb^{3+} with the characteristic energy transfer UC, excited state absorption and UC emissions of the LZO:Er,Yb NPs under 980 nm excitation. ET, ESA, GSA and BET represent energy transfer, excited state absorption, ground state absorption and back energy transfer, respectively.

followed by the blue radiative emission from Tm^{3+} ion due to blue ($^1D_2 \rightarrow {}^3F_4$ and $^1G_4 \rightarrow {}^3H_6$) and UV ($^1I_6/^3P_0 \rightarrow {}^3H_6$, $^1I_6/^3P_0 \rightarrow {}^3F_4$, and $^1D_2 \rightarrow {}^3H_6$) transitions.

Unlike Yb^{3+} ions, Gd^{3+} ions can not directly absorb 980 nm

photons due to the large energy bandgap between its ground state and the first excited state. Apparently in the tridoped LZO NPs with Tm^{3+}, Gd^{3+}, and Yb^{3+} ions, the energy transfer $^3P_{2,1} \rightarrow {}^3H_6$ (Tm^{3+}) : $^8S_{7/2} \rightarrow {}^6I_j$ (Gd^{3+}) populates the excited ^6I_j states of Gd^{3+}. Given that the
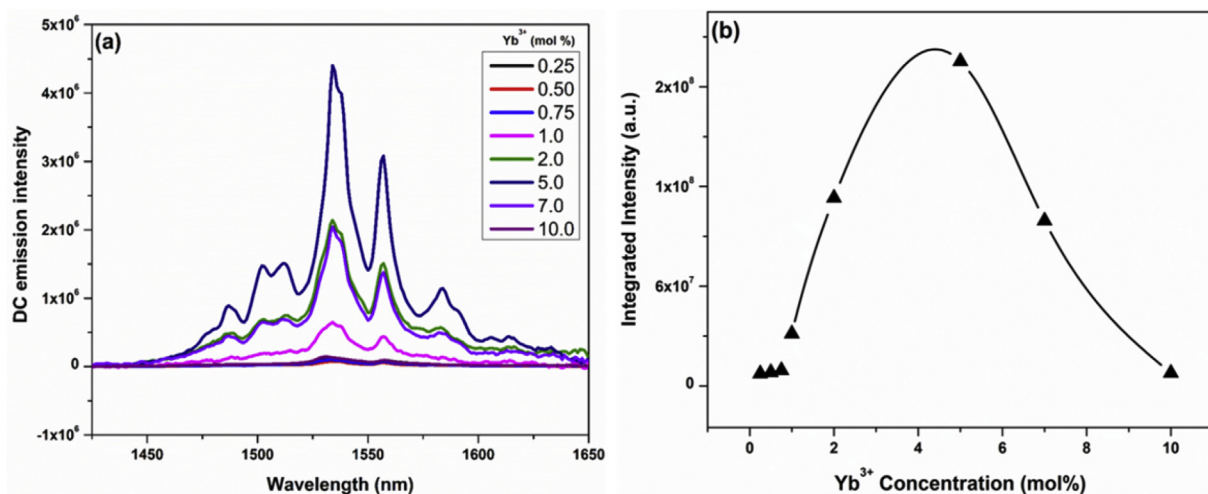
Fig. 4. The LZO:3%Er,y%Yb NPs: (a) DC emission spectra and (b) the variation of DC emission intensity as a function of Yb^{3+} doping concentration.
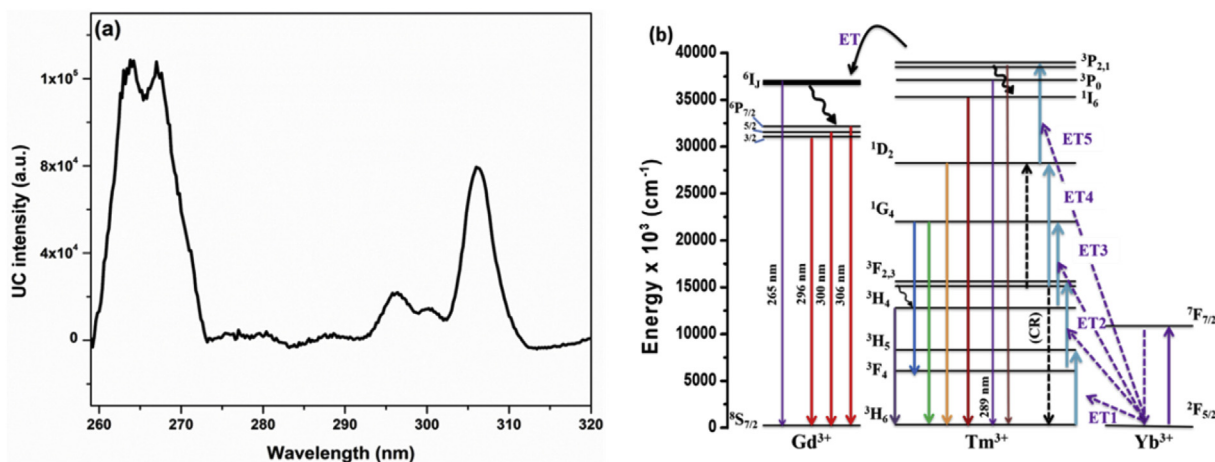

Fig. 5. (a) UC emission spectra of the LZO:20%Yb,1%Tm,20%Gd NPs and (b) Energy levels diagram of Yb^{3+}, Tm^{3+} and Gd^{3+} with proposed mechanisms of the UC emissions under 980 nm excitation.
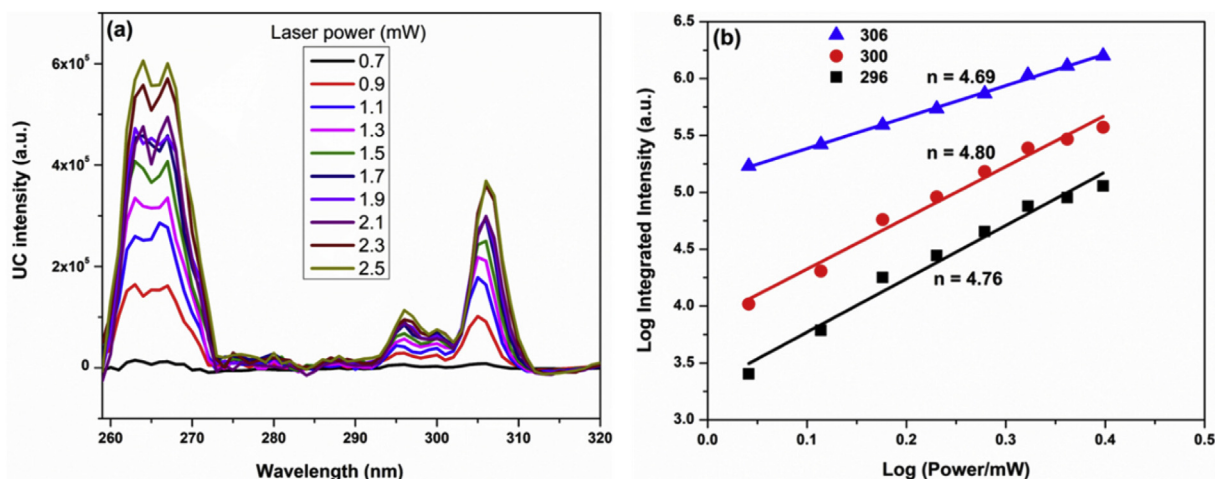

Fig. 6. (a) UC emission spectra at different laser powers, (b) log–log plot of UC emission intensity versus laser power of three emission bands at 310 nm (sphere symbol), 295 nm (triangle) and 265 nm (square).

probabiltiy of nonradiative transition from $^6I_{7/2}$ level to the $^6P_{5/2}$ level in Gd^{3+} is 5 times that of $^6I_{7/2} \rightarrow {}^8S_{7/2}$ radiative transition, the non-radiative decay $^6I_J \rightarrow {}^6P_J$ results in $^6P_J \rightarrow {}^8S_{7/2}$ emissions [67]. So Gd^{3+} emssion was detected when the excited states ^6I_J and/or ^6P_J radiatively

depopulate to the ground state. We can conclude based on above dis-cussion that the population of the $^3P_{1,2}$ levels is important for strong UVUC from the LZO:20%Yb,1%Tm,20%Gd NPs.

The UV UC laser power dependence spectra display gradual increase

of emission intensity with increasing laser power (Fig. 6a). Moreover, the log*I* *vs* log*P* plots (Fig. 6b) exhibit linear dependency with slopes of approximately 4.69, 4.80, and 4.76 for the 306, 300, and 296 nm emissions, respectively, indicating five-photon processes, similar to those reported for other phosphor systems [31,32].

4. Conclusion

In this work, LZO NPs were doubly doped with 3%Er^{3+} and y% Yb^{3+} for visible upconversion and NIR-B downconversion processes using a molten salt synthesis method. The effect of Yb^{3+} doping level was investigated on the UC and DC intensity of the LZO:3%Er:y%Yb NPs. As the concentration of Yb^{3+} dopant was increased, the orderliness degree of the pyrochlore phase and the particle size decreased. Similarly, triple doping of the LZO NPs with 20% Yb, 1% Tm, and 20% Gd was used to explore for ultraviolet upconversion. Power dependence emission intensity revealed that the VUC proceeds by 2-photon absorption whereas the UVUC via 5-photon absorption. The mechanisms of these three photoluminescence operations were explained in detail by various energy transfer processes. These pyrochlore NPs displaying visible UC, near IR B DC and ultraviolet UC are expected to be highly feasible for bioimaging and water disinfection. We still need to look out for various design strategies to improve the upconversion efficiency to make such materials more practical to be commercialized.

Acknowledgement

Appendix A. Supplementary data

Supplementary data to this article can be found online at https://doi.org/10.1016/j.jlumin.2019.116591.

References

[1] G. Zhang, F. Song, C. Ming, Y. Yu, C. Zhang, HongyanZhao, Q. Wanga, J. Liu, Photoluminescence properties and pump-saturation effect of Er^{3+}/Yb^{3+} co-doped Y$_2$Ti$_2$O$_7$ nanocrystals, J. Lumin. 132 (2012) 774–779.

[2] J. Jadczak, L. Bryja, J. Kutrowska-Girzycka, P. Kapuściński, M. Bieniek, Y.S. Huang, P. Hawrylak, Room temperature multi-phonon upconversion photoluminescence in monolayer semiconductor WS$_2$, Nat. Commun. 10 (1) (2019) 107.

[3] F. Auzel, Upconversion and anti-Stokes processes with f and d ions in solids, Chem. Rev. 104 (1) (2004) 139–174.

[4] J.-C.G. Bunzli, Lanthanide luminescence for biomedical analyses and imaging, Chem. Rev. 110 (5) (2010) 2729–2755.

[5] J.S. Chivian, W.E. Case, D.D. Eden, The photon avalanche: a new phenomenon in Pr^{3+}-based infrared quantum counters, Appl. Phys. Lett. 35 (2) (1979) 124.

[6] E. Nakazawa, S. Shionoya, Cooperative luminescence in YbPO$_4$, Phys. Rev. Lett. 25 (25) (1970) 1710.

[7] R.R. Deng, F. Qin, R.F. Chen, W. Huang, M.H. Hong, X.G. Liu, Temporal fullcolour tuning through non-steady-state upconversion, Nat. Nanotechnol. 10 (2015) 237–242.

[8] D. Pugliese, N.G. Boetti, J. Lousteau, E. Ceci-Ginistrelli, E. Bertone, F. Geobaldo, D. Milanese, Concentration quenching in an Er-doped phosphate glass for compact optical lasers and amplifiers, J. Alloy. Comp. 657 (2016) 678–683.

[9] Y.Y. Cheng, A. Nattestad, T.F. Schulze, R.W. MacQueen, B. Fückel, K.L., G.G. Wallace, T. Khoury, M.J. Crossley, T.W. Schmidt, Increased upconversion performance for thin film solar cells: a trimolecular composition, Chem. Sci. 7 (2016) 559–568.

[10] M. Pokhrel, C. Valdes, Y. Mao, Ultraviolet upconversion enhancement in triply doped NaYF$_4$: Tm$_{3p}$, Yb$_{3p}$ particles: the role of Nd$_{3p}$ or Gd$_{3p}$ Co-doping, Opt. Mater. 58 (2016) 67–75.

[11] L. Shang, S. Dong, G.U. Nienhaus, Ultra-small fluorescent metal nanoclusters: synthesis and biological applications, Nano Today 6 (2011) 401–418.

[12] J. Pichaandi, J.C. Boyer, K.R. Delaney, F. C. J. M. v. Veggel, Two-photon upconversion laser (scanning and wide-field) microscopy using Ln$_{3p}$-doped NaYF$_4$ upconverting nanocrystals: a critical evaluation of their performance and potential in

[13] L. Li, C.F. Guo, S. Jiang, D.K. Agrawalc, T. Li, Green up-conversion luminescence of Yb^{3+}-Er^{3+} co-doped CaLa$_2$ZnO$_5$ for optically temperature sensing, RSC Adv. 4 (2014) 6391–6396.

[14] A. Pandey, V.K. Rai, V. Kumar, V. Kumar, H.C. Swart, Upconversion based temperature sensing ability of Er^{3+}-Yb^{3+} codoped SrWO$_4$: an optical heating phosphor, Sens. Actuators, B 209 (2015) 352–358.

[15] D. Birtalan, W. Nunley, Optoelectronics: Infrared-Visable-Ultraviolet Devices and Applications, CRC Press, 2009.

[16] G. Galleani, S.H. Santagneli, Y. Ledemi, Y. Messaddeq, O. Janka, R. Pöttgen, H. Eckert, Ultraviolet upconversion luminescence in a highly transparent triply-doped Gd^{3+}–Tm^{3+}–Yb^{3+} fluoride–phosphate glasses, J. Phys. Chem. C 122 (4) (2018) 2275–2284.

[17] C., B. J, M., v. V. F. C. J, Absolute quantum yield measurements of colloidal NaYF$_4$: Er^{3+}, Yb^{3+} upconverting nanoparticles, Nanoscale 2 (2010) 1417–1419.

[18] F., W, J., W, X., L, Direct evidence of a surface quenching effect onsize-dependent luminescence of upconversion nanoparticles, Angew. Chem. Int. Ed. 49 (2010) 7456–7460.

[19] L., T, X., L, F., W, H., Z, Excitation energy migration dynamics in upconversion nanomaterials, Chem. Soc. Rev. 44 (2015) 1331–1345.

[20] X., C, D., P, Q., J, F., W, Photon upconversion in core-shell nanoparticles, Chem. Soc. Rev. 44 (2015) 1318–1330.

[21] A. Urbina-Frías, T. L_opez-Luke, H. Desirena, P.S., A. Torres-Castro, E. D. l. Rosa, Switching green to red emission in tridoped ZrO$_2$:Yb^{3+}-Er^{3+}-Bi^{3+} nanocrystals, Opt. Mater. 48 (2015) 92–96.

[22] X.X. Yang, Z.L. Fu, Y.M. Yang, C.P. Zhang, Z.J. Wu, T.Q. Sheng, Optical temperature sensing behavior of high-efficiency upconversion: Er^{3+}–Yb^{3+} Co-Doped NaY (MoO$_4$)$_2$ phosphor, J. Am. Ceram. Soc. 98 (2015) 2595–2600.

[23] G. Zhang, F. Song, C. Ming, Y. Yu, C. Zhang, HongyanZhao, Q. Wanga, J. Liu, Photoluminescence properties and pump-saturation effect of Er^{3+}/Yb^{3+} co-doped Y$_2$Ti$_2$O$_7$ nanocrystals, J. Lumin. 132 (2012) 774–779.

[24] R.V. Perrella, I.C. Ribeiro, P.H.A. Campos-Junior, M.A. Schiavon, E. Pecoraro, S.J.L. Ribeiro, J.L. Ferrari, CaTiO$_3$:Er^{3+}:Yb^{3+} upconversion from 980 nm to 1550 nm excitation and its potential as cells luminescent probes, Mater. Chem. Phys. 223 (2019) 391–397.

[25] M. Pokhrel, C. Valdes, Y. Mao, Ultraviolet upconversion enhancement in triply doped NaYF$_4$:Tm^{3+},Yb^{3+} particles: the role of Nd^{3+} or Gd^{3+} Co-doping, Opt. Mater. 58 (2016) 67–75.

[26] T. Jiang, Y. Liu, S. Liu, N. Liu, W. Qin, Upconversion emission enhancement of Gd^{3+} ions induced by surface plasmon field in Au@NaYF$_4$ nanostructures codoped with Gd^{3+}–Yb^{3+}–Tm^{3+} ions, J. Colloid Interface Sci. 377 (1) (2012) 81–87.

[27] C. Cao, W. Qin, J. Zhang, Study on up-conversion emissions of Er^{3+}/Tm^{3+} co-doped GdF$_3$ and NaGdF$_4$, Optic Commun. 283 (4) (2010) 547–550.

[28] F. Güell, R. Solé, J. Gavaldà, M. Aguiló, M. Galán, F. Díaz, J. Massons, Upconversion luminescence of Tm^{3+} sensitized by Yb^{3+} ions in monoclinic KGd(WO$_4$)$_2$ single crystals, Opt. Mater. 30 (2) (2007) 222–226.

[29] F. Pandozzi, F. Vetrone, J.-C. Boyer, R. Naccache, J.A. Capobianco, A. Speghini, M. Bettinelli, A spectroscopic analysis of blue and ultraviolet upconverted emissions from Gd$_3$Ga$_5$O$_{12}$:Tm^{3+},Yb^{3+} nanocrystals, J. Phys. Chem. B 109 (37) (2005) 17400–17405.

[30] C. He, D. Zhao, G. Qin, K. Zheng, W. Qin, Enhanced ultraviolet upconversion luminescence of Tm and Yb codoped ZrF$_4$–BaF$_2$–LaF$_3$–AlF$_3$–NaF glass, J. Nanosci. Nanotechnol. 11 (11) (2011) 9494–9497.

[31] K. Zheng, Z. Liu, C. Lv, W. Qin, Temperature sensor based on the UV upconversion luminescence of Gd^{3+} in Yb^{3+}–Tm^{3+}–Gd^{3+} codoped NaLuF$_4$ microcrystals, J. Mater. Chem. C 1 (35) (2013) 5502–5507.

[32] C. Cao, W. Qin, J. Zhang, Y. Wang, P. Zhu, G. Wei, G. Wang, R. Kim, L. Wang, Ultraviolet upconversion emissions of Gd^{3+}, Opt. Lett. 33 (8) (2008) 857–859.

[33] C. Li, Y. Zhang, M. Wang, Y. Zhang, G. Chen, L. Li, D. Wu, Q. Wang, In vivo real-time visualization of tissue blood flow and angiogenesis using Ag$_2$S quantum dots in the NIR-II window, Biomaterials 35 (1) (2014) 393–400.

[34] S. Diao, J.L. Blackburn, G. Hong, A.L. Antaris, J. Chang, J.Z. Wu, B. Zhang, K. Cheng, C.J. Kuo, H. Dai, Fluorescence imaging in vivo at wavelengths beyond 1500 nm, Angew. Chem. Int. Ed. 54 (49) (2015) 14758–14762.

[35] G. Hong, Y. Zou, A.L. Antaris, S. Diao, D. Wu, K. Cheng, X. Zhang, C. Chen, B. Liu, Y. He, J.Z. Wu, J. Yuan, B. Zhang, Z. Tao, C. Fukunaga, H. Dai, Ultrafast fluorescence imaging in vivo with conjugated polymer fluorophores in the second near-infrared window, Nat. Commun. 5 (2014) 4206.

[36] A. Nadort, J. Zhao, E.M. Goldys, Lanthanide upconversion luminescence at the nanoscale: fundamentals and optical properties, Nanoscale 8 (27) (2016) 13099–13130.

[37] A.L. Rogach, A. Eychmüller, S.G. Hickey, S.V. Kershaw, Infrared-emitting colloidal nanocrystals: synthesis, assembly, spectroscopy, and applications, Small 3 (4) (2007) 536–557.

[38] K. Welsher, Z. Liu, S.P. Sherlock, J.T. Robinson, Z. Chen, D. Daranciang, H. Dai, A route to brightly fluorescent carbon nanotubes for near-infrared imaging in mice, Nat. Nanotechnol. 4 (2009) 773.

[39] G. Hong, J.C. Lee, J.T. Robinson, U. Raaz, L. Xie, N.F. Huang, J.P. Cooke, H. Dai, Multifunctional in vivo vascular imaging using near-infrared II fluorescence, Nat. Med. 18 (2012) 1841.

[40] J.T. Robinson, K. Welsher, S.M. Tabakman, S.P. Sherlock, H. Wang, R. Luong, H. Dai, High performance in vivo near-IR (> 1 μm) imaging and photothermal cancer therapy with carbon nanotubes, Nano Res. 3 (11) (2010) 779–793.

[41] J. Zhao, D. Zhong, S. Zhou, NIR-I-to-NIR-II fluorescent nanomaterials for biomedical imaging and cancer therapy, J. Mater. Chem. B 6 (3) (2018) 349–365.

[42] D.J. Naczynski, M.C. Tan, M. Zevon, B. Wall, J. Kohl, A. Kulesa, S. Chen, C.M. Roth,

R.E. Riman, P.V. Moghe, Rare-earth-doped biological composites as in vivo short-wave infrared reporters, Nat. Commun. 4 (2013) 2199.

[43] S.K. Gupta, M. Abdou, J.P. Zuniga, P.S. Ghosh, E. Molina, B. Xu, M. Chipara, Y. Mao, Roles of oxygen vacancies and pH induced size changes on photo- and radioluminescence of undoped and Eu^{3+}-doped $La_2Zr_2O_7$ nanoparticles, J. Lumin. 209 (2019) 302–315.

[44] R.A. Hansel, S.K. Desai, S.W. Allison, A.L. Heyes, D.G. Walker, Emission lifetimes of europium-doped pyrochlores for phosphor thermometry, J. Appl. Phys. 107 (1) (2010) 016101.

[45] M. Abdou, S.K. Gupta, J.P. Zuniga, Y. Mao, On structure and phase transformation of uranium doped $La_2Hf_2O_7$ nanoparticles as an efficient nuclear waste host, Materials Chemistry Frontiers 2 (12) (2018) 2201–2211.

[46] S.K. Gupta, M. Abdou, P.S. Ghosh, J.P. Zuniga, Y. Mao, Thermally induced disorder–order phase transition of $Gd_2Hf_2O_7$:Eu^{3+} nanoparticles and its implication on photo- and radioluminescence, ACS Omega 4 (2) (2019) 2779–2791.

[47] K.A. Sakharov, E.P. Simonenko, N.P. Simonenko, M.L. Vaganova, Y.E. Lebedeva, A.S. Chaynikova, I.V. Osin, O.Y. Sorokin, D.V. Grashchenkov, V.G. Sevastyanov, N.T. Kuznetsov, E.N. Kablov, Glycol-citrate synthesis of fine-grained oxides $La_{2-x}Gd_xZr_2O_7$ and preparation of corresponding ceramics using FAST/SPS process, Ceram. Int. 44 (7) (2018) 7647–7655.

[48] F. Yang, Y. Wang, X. Zhao, P. Xiao, Enhanced ionic conductivity in pyrochlore and fluorite mixed phase yttrium-doped lanthanum zirconate, J. Power Sources 273 (2015) 290–297.

[49] F. Zhong, J. Zhao, L. Shi, Y. Xiao, G. Cai, Y. Zheng, J. Long, Alkaline-Earth metals-doped pyrochlore $Gd_2Zr_2O_7$ as oxygen conductors for improved NO_2 sensing performance, Sci. Rep. 7 (1) (2017) 4684.

[50] S. Zhang, H.B. Zhang, F.A. Zhao, M. Jiang, H.Y. Xiao, Z.J. Liu, X.T. Zu, Impact of isovalent and aliovalent substitution on the mechanical and thermal properties of $Gd_2Zr_2O_7$, Sci. Rep. 7 (1) (2017) 6399.

[51] N.M. Sangeetha, F.C.J.M. van Veggel, Lanthanum silicate and lanthanum zirconate nanoparticles Co-doped with Ho^{3+} and Yb^{3+}: matrix-dependent red and green upconversion emissions, J. Phys. Chem. C 113 (33) (2009) 14702–14707.

[52] S.K. Gupta, J.P. Zuniga, M. Abdou, Y. Mao, Thermal annealing effects on $La_2Hf_2O_7$:Eu^{3+} nanoparticles: a curious case study of structural evolution and site-specific photo- and radio-luminescence, Inorganic Chemistry Frontiers 5 (10) (2018) 2508–2521.

[53] S.K. Gupta, J.P. Zuniga, P.S. Ghosh, M. Abdou, Y. Mao, Correlating structure and luminescence properties of undoped and Eu^{3+}-doped $La_2Hf_2O_7$ nanoparticles prepared with different coprecipitating pH values through experimental and theoretical studies, Inorg. Chem. 57 (18) (2018) 11815–11830.

[54] J. Liao, L. Nie, S. Liu, B. Liu, H.-r. Wen, Yb^{3+} concentration dependence of up-conversion luminescence in $Y_2Sn_2O_7$:Yb^{3+}/Er^{3+} nanophosphors, J. Mater. Sci. 49 (17) (2014) 6081–6086.

[55] C. Mi, J. Wu, Y. Yang, B. Han, J. Wei, Efficient upconversion luminescence from $Ba_5Gd_8Zn_4O_{21}$:Yb^{3+},Er^{3+} based on a demonstrated cross-relaxation process, Sci. Rep. 6 (2016) 22545.

[56] Z. Chen, T. Chen, W. Gong, W. Xu, D. Wang, Q. Wang, Effect of Li^+ ions doping on microstructure and upconversion emission of $Y_2Ti_2O_7$:Er^{3+}/Yb^{3+} nanophosphors synthesized via a sol–gel method, J. Am. Ceram. Soc. 96 (6) (2013) 1857–1862.

[57] Z. Chen, W. Gong, T. Chen, S. Li, D. Wang, Q. Wang, Preparation and upconversion luminescence of Er^{3+}/Yb^{3+} codoped $Y_2Ti_2O_7$ nanocrystals, Mater. Lett. 68 (2012) 137–139.

[58] F. Shi, Y. Zhao, Sub-10 nm and monodisperse β-$NaYF_4$:Yb,Tm,Gd nanocrystals with intense ultraviolet upconversion luminescence, J. Mater. Chem. C 2 (12) (2014) 2198–2203.

[59] M. Pokhrel, S.K. Gupta, K. Wahid, Y. Mao, Pyrochlore rare-earth hafnate $RE_2Hf_2O_7$ (RE = La and Pr) nanoparticles stabilized by molten-salt synthesis at low temperature, Inorg. Chem. 58 (2) (2019) 1241–1251.

[60] N. Garg, K.K. Pandey, C. Murli, K.V. Shanavas, B.P. Mandal, A.K. Tyagi, S.M. Sharma, Decomposition of lanthanum hafnate at high pressures, Phys. Rev. B 77 (21) (2008) 214105.

[61] F. Vetrone, J.-C. Boyer, J.A. Capobianco, A. Speghini, M. Bettinelli, Significance of Yb^{3+} concentration on the upconversion mechanisms in codoped Y_2O_3:Er^{3+},Yb^{3+} nanocrystals, J. Appl. Phys. 96 (1) (2004) 661–667.

[62] G. Lakshminarayana, E.M. Weis, A.C. Lira, U. Caldiño, D.J. Williams, M.P. Hehlen, Cross Relaxation in rare-earth-doped oxyfluoride glasses, J. Lumin. 139 (2013) 132–142.

[63] Y. Yang, Z. Yang, P. Li, X. Li, Q. Guo, B. Chen, Dependence of optical properties on the composition in Er^{3+}-doped $xNaPO_3$–(80−x)TeO_2–10ZnO–10Na_2O glasses, Opt. Mater. 32 (1) (2009) 133–138.

[64] R.V. Perrella, M.A. Schiavon, E. Pecoraro, S.J.L. Ribeiro, J.L. Ferrari, Broadened band C-telecom and intense upconversion emission of Er^{3+}/Yb^{3+} co-doped $CaYAlO_4$ luminescent material obtained by an easy route, J. Lumin. 178 (2016) 226–233.

[65] R.J. Thrash, L.F. Johnson, Upconversion laser emission from Yb^{3+}-sensitized Tm^{3+} in BaY_2F_8, J. Opt. Soc. Am. B 11 (5) (1994) 881–885.

[66] X. Chen, Z. Song, Study on six-photon and five-photon ultraviolet upconversion luminescence, J. Opt. Soc. Am. B 24 (4) (2007) 965–971.

[67] J. Sytsma, G.F. Imbusch, G. Blasse, The decay of the $^6I_{7/2}$ term level of Gd^{3+} in YOCl and LiYF_4, J. Phys. Condens. Matter 2 (23) (1990) 5171–5178.